Interaction and Multiscale Mechanics, Vol. 4, No. 3 (2011) 187-206
DOI: http://dx.doi.org/10.12989/imm.2011.4.3.187

Analysis of post-failure response of sands using a critical state micropolar plasticity model

Majid T. Manzari* and Karma Yonten

Civil and Environmental Engineering Department, The George Washington University, Washington, DC 20052, USA

(Received December 1, 2010, Accepted April 7, 2011)

Abstract. Accurate estimations of pre-failure deformations and post-failure responses of geostructures require that the simulation tool possesses at least three main ingredients: 1) a constitutive model that is able to describe the macroscopic stress-strain-strength behavior of soils subjected to complex stress/strain paths over a wide range of confining pressures and densities, 2) an embedded length scale that accounts for the intricate physical phenomena that occur at the grain size scale in the soil, and 3) a computational platform that allows the analysis to be carried out beyond the development of an initially "contained" failure zone in the soil. In this paper, a two-scale micropolar plasticity model will be used to incorporate all these ingredients. The model is implemented in a finite element platform that is based on the mechanics of micropolar continua. Appropriate finite elements are developed to couple displacement, micro-rotations, and pore-water pressure in form of u_n-ϕ_m and u_n-p_m-ϕ_m ($n > m$) elements for analysis of dry and saturated soils. Performance of the model is assessed in a biaxial compression test on a slightly heterogeneous specimen of sand. The role of micropolar component of the model on capturing the post-failure response of the soil is demonstrated.

Keywords: post-failure response; granular soil; micropolar plasticity; localization; shear banding.

1. Introduction

Development of a unified approach for the analysis of pre- and post-failure response of geostructures has been the focus of intense research in recent years. In the pre-failure regime, shear-induced volume change (dilatancy) is a key quantity that governs the response of granular soils in most geostructures. It has been long recognized that dilatancy evolves during the shearing process and gradually ceases as the soil reaches a critical state condition. The evolving nature of dilatancy appears in both monotonic and reverse loading conditions (e.g. Manzari and Dafalias 1997, Dafalias and Manzari 2004) and is closely related to the void ratio and confining pressure of the soil. However as the soil approaches critical state, the heterogeneous distributions of void ratio and stresses within the soil mass as well as the boundary conditions of the soil mass may lead to the emergence of highly localized shear zones. The soil within these localized zones gradually approaches a critical state condition while the material outside these zones may undergo an entirely

* Corresponding author, Professor, E-mail: manzari@gwu.edu

different mode of deformation. Thickness of the localized zone (e.g. shear band) normally depends on the average grain size of the soil and may evolve during the shearing process. It has been observed that within the shear band soil grains may undergo significant rotations (Viggiani *et al.* 2010). The energy dissipation due to the grain rotations cannot be included in constitutive models that are formulated in the framework of classical continuum. A suitable framework for granular soils is the micropolar continuum in which any point of the medium undergoes displacements and rotations. This approach has been used by many researchers to model shear localization in granular soils (Vardoulakis and Sulem 1995). Manzari (2004) has used a micropolar version of Mohr-Coulomb plasticity model to assess the post-failure response of granular soils in a number of geomechanics problems ranging from retaining walls to shallow footings and deep excavations. Alsaleh *et al.* (2006) have developed a micropolar extension of the plasticity model by Lade and Kim (1998). Alshibli *et al.* (2006) have used this model to assess shear localization of Ottawa sand in biaxial compression test. Alsaleh *et al.* (2009) used the model presented in Alsaleh *et al.* (2006) to study strain localization and failure in geo-synthetice reinforced soil structures. In addition to elastoplastic models, numerous applications of micropolar hypoplastic models have been reported in literature (e.g. Huang and Bauer 2003, among others). The vast majority of existing micropolar models are formulated for classical plasticity models (such as Drucker-Parger and Mohr Coulomb, or variations of these models) in which prediction of soil dilation is excessive and critical state of granular material is not considered. Moreover the majority of micropolar elastoplastic models available in literature are unable to capture the response of granular soils in reverse loading.

This paper presents the implementation of a critical state micropolar plasticity model in a fully-coupled effective stress-based framework. The model is a micropolar extension (Manzari and Dafalias 2005) of the critical state two-surface plasticity model proposed by Manzari and Dafalias (1997) and Dafalias and Manzari (2004). The model inherits the capabilities of its nonpolar counterpart that is shown to capture the essential features of response of sands in monotonic and cyclic loading regimes with a single set of parameters (Manzari and Dafalias 1997, Dafalias and Manzari 2004). The proposed micropolar formulation and the extended constitutive model are used to investigate the response of a slightly heterogeneous granular soil specimen in biaxial compression tests.

2. Micropolar continuum

2.1 Kinematics

At any material point of the continuum, we consider both a displacement and a rotation vector denoted by $\mathbf{u}$ and $\boldsymbol{\phi}$, respectively. The Cosserat micro-rotation $\mathbf{R}$ relates the current state of a triad of orthonormal directions attached to each material point to its initial state (Forest 2001), i.e.

$$\mathbf{R} = \mathbf{I}_2 - \boldsymbol{\Gamma} \cdot \boldsymbol{\phi} \tag{1}$$

where $\mathbf{I}_2$ is the second rank unit tensor, and $\boldsymbol{\Gamma}$ is the permutation tensor is the permutation tensor defined as

$$\Gamma_{ijk} = 0 \quad \text{for} \quad i = j, \quad j = k \quad \text{or} \quad k = i$$

$$\Gamma_{ijk} = 1 \quad \text{for} \quad (i,j,k) \in \{(1,2,3),(2,3,1),(3,1,2)\}$$

$$\Gamma_{ijk} = -1 \quad \text{for} \quad (i,j,k) \in \{(1,3,2),(3,2,1),(2,1,3)\}$$

The associated Cosserat deformation $\boldsymbol{\varepsilon}$ and curvature tensor $\boldsymbol{\kappa}$ are written as

$$\boldsymbol{\varepsilon} = \nabla \mathbf{u} - \Gamma \cdot \boldsymbol{\phi}; \qquad \boldsymbol{\kappa} = \nabla \boldsymbol{\phi} \tag{2}$$

It is clear that in the absence of rotation vector, $\boldsymbol{\phi}$, classical continuum mechanics is recovered.

2.2 Balance laws

It is assumed that the transfer of interaction between two parts of the continuum through a surface element $\mathbf{n}dS$ ($\mathbf{n}$ is the normal to the surface element) occurs by means of both a traction vector $\mathbf{t}dS$ and a moment vector, $\mathbf{m}dS$. Surface forces and couples are represented by the generally non-symmetric force-stress and couple-stress tensors $\boldsymbol{\sigma}$, and $\boldsymbol{\mu}$, respectively (Forest 2001).

$$\mathbf{t} = \boldsymbol{\sigma} \cdot \mathbf{n} \qquad \mathbf{m} = \boldsymbol{\mu} \cdot \mathbf{n} \tag{3}$$

The axioms of balance of linear momentum and moment of momentum require that the following equations hold

$$\sigma_{ji,j} + f_i = \rho \ddot{u}_i$$

$$\mu_{ji,j} + \Gamma_{ikl}\sigma_{kl} + \zeta_i = I\ddot{\phi}_i \tag{4}$$

in which $\mathbf{f}$ and ζ, respectively, represent vectors of body forces and body couples, ρ is mass density and I denotes the isotropic rotational inertia.

In a fully-coupled effective stress formulation, in addition to the balance laws for the soil skeleton given by Eq. (4), conservation of mass equation is required for the pore fluid. The local form of mass conservation is given by

$$V_{i,i} - \dot{\varepsilon}_{ii} = 0 \tag{5}$$

in which v_i is the components of fluid velocity and ε_{ii} is volumetric strain of the soil. The fluid velocity, according to Darcy's law, is given as

$$v_i = -\frac{k_{ij}}{\gamma_w}(p_{,j} + b_j) \tag{6}$$

where k_{ij}, p, b_i, and γ_w are the tensor of coefficient of permeability, pore water pressure, body force due to water, and unit weight of water respectively. The fluid flux q is defined by

$$q = \mathbf{v} \cdot \mathbf{n} \tag{7}$$

where $\mathbf{n}$ is the outward unit normal to the surface on which the flux is computed. In a specific boundary value problem, appropriate additional boundary conditions should be defined to accompany Eqs. (3)-(7).

3. Constitutive model

Solution of a geomechanics boundary value problem governed by Eq. (4) requires proper formulation of the constitutive equations linking the deformation and curvature tensors to the force-stresses and couple-stresses. In a fully-coupled analysis effective force-stresses are used in the constitutive equations. Here we will use an elastoplastic constitutive model that is suitable for granular materials. Details of this constitutive model, previously proposed by Manzari and Dafalias (2005), are outlined in the following subsections.

3.1 Additive decomposition

Assuming small perturbations, the deformation and curvature tensors are decomposed to an elastic part denoted by a superscript "*e*" and a plastic part indicated by a superscript "*p*".

$$\dot{\boldsymbol{\varepsilon}} = \dot{\boldsymbol{\varepsilon}}^e + \dot{\boldsymbol{\varepsilon}}^p; \qquad \dot{\boldsymbol{\kappa}} = \dot{\boldsymbol{\kappa}}^e + \dot{\boldsymbol{\kappa}}^p \tag{8}$$

3.2 Elastic response

The general isotropic elastic relationships for a micropolar continuum are given as (Nowacki 1986)

$$\begin{aligned} \dot{\sigma}_{ij} &= \lambda \dot{\varepsilon}^e_{kk}\delta_{ij} + 2G\dot{\varepsilon}^e_{(ij)} + 2G_c\dot{\varepsilon}^e_{\{ij\}} \\ \dot{\mu}_{ij} &= \alpha \dot{\kappa}^e_{kk}\delta_{ij} + 2\beta\dot{\kappa}^e_{(ij)} + 2\gamma\dot{\kappa}^e_{\{ij\}} \end{aligned} \tag{9}$$

Where $\dot{\varepsilon}_{(ij)}$ and $\dot{\varepsilon}_{\{ij\}}$, respectively, denote the symmetric and skew symmetric parts of $\dot{\varepsilon}_{ij}$, while $\dot{\kappa}_{(ij)}$ and $\dot{\kappa}_{\{ij\}}$ represent the symmetric and skew symmetric parts of $\dot{\kappa}_{ij}$. In addition to the usual Lame constants (λ and $G = \mu$), Cosserat couple modulus (G_c), and three additional elasticity moduli (α, β, and γ) appear in Eq. (9). In order to simplify the elastic relations, we consider: $\alpha = \beta = 0$ and

$$\gamma = \frac{2GG_c}{G + G_c} l_1^2 \tag{10}$$

where l_1 is a characteristic length. Hence, a simplified form of Eq. (9) is obtained as follows

$$\begin{aligned} \dot{\sigma}_{ij} &= \lambda \dot{\varepsilon}^e_{kk}\delta_{ij} + (G + G_c)\dot{\varepsilon}^e_{ij} \\ \dot{\mu}_{ij} &= \gamma \dot{\kappa}^e_{ij} \end{aligned} \tag{11}$$

in which the first equation reduces to Hooke's law for isotropic elasticity in the absence of Cosserat rotation (i.e. when strain tensor is symmetric). Given the above assumptions, we note that the curvature tensor $\boldsymbol{\kappa}$ and couple stress tensor $\boldsymbol{\mu}$ are both symmetric, otherwise their skew symmetric parts would be undetermined.

In accordance with the critical state two-surface plasticity model for sands (Dafalias and Manzari 2004) the standard Lame parameters λ and μ (same as the shear modulus G) are obtained from the following equations, which indicate the pressure dependence nature of elastic moduli, reflecting a

key characteristic of geomaterials.

$$G = G_0 p_{at} \frac{(2.97 - e)^2}{1 + e} \left(\frac{p}{p_{at}} \right)^{1/2}; \qquad \lambda = \frac{2\nu}{1 - 2\nu} G \tag{12}$$

where p_{at} is atmospheric pressure, p is mean effective stress, e is current void ratio, ν is Poisson's ratio, and G_0 is a model constant.

3.3 Yield function

The yield function is assumed to have the following form

$$f = [\tilde{J}_2]^{1/2} - \sqrt{2/3} pm \tag{13}$$

where $\tilde{J}_2$ is now defined as

$$\tilde{J}_2 = a_1 \tilde{s}_{ij} \tilde{s}_{ij} + a_2 \tilde{s}_{ij} \tilde{s}_{ji} + b_1 \mu_{ij} \mu_{ij} + b_2 \mu_{ij} \mu_{ji} \tag{14a}$$

in which $\tilde{s}_{ij} = s_{ij} - p\alpha_{ij}$, where $s_{ij} = \sigma_{ij} - p\delta_{ij}$ is the deviatoric (force-) stress tensor and α is an unsymmetric deviatoric tensor defined as a tensor of internal variables. Parameter "m" indicates the size of the yield surface that is assumed to be constant in the present formulation. Parameters a_1, a_2, b_1, and b_2 may be calculated on the basis of micromechanical consideration of particles displacements and rotations in a granular medium (Vardoulakis and Sulem 1995). Here a specific form of Eq. (14a) is selected by considering the following parameters

$$a_1 = 1,\ a_2 = 0,\ b_1 = \frac{1}{l_2^2},\ b_2 = 0$$

where l_2 is a second characteristic length, corresponding to plastic deformation. This means

$$\tilde{J}_2 = (\tilde{s}_{ij} \tilde{s}_{ij}) + \frac{1}{l_2^2} \mu_{ij} \mu_{ij} \tag{14b}$$

Here we note that one may choose $l_2 = l_1$, but we keep the option of choosing different values for and l_1 and l_2. The underlying assumption for this choice is that in comparison to the length scale affecting plastic deformations in granular materials the length scale in elastic regime is manifested by deformation mechanisms that occur within a smaller zone around the point of interest. This assumption requires further verification by experimental and possibly computational observations using, for example, discrete element simulations.

3.4 Flow rule

A non-associative flow rule, similar to the flow rule proposed in Manzari and Dafalias (1997), is adopted as follows

$$\dot{\boldsymbol{\varepsilon}}^p = \langle L \rangle \mathbf{R}^{\sigma}; \qquad \dot{\boldsymbol{\kappa}}^p = \langle L \rangle \mathbf{R}^{\mu} \tag{15}$$

where L is the loading index, and symbol $< >$ indicates the Macauley bracket ($<L> = 0$, for $L < 0$ or $L = 0$, and $<L> = L$ for $L > 0$). Furthermore, directions of plastic strains and plastic curvatures are

indicated through the following two tensors (R^{σ} and R^{μ})

$$\mathbf{R}^{\sigma} = \mathbf{n}^{\sigma} + \frac{1}{3}\mathbf{D}\mathbf{I}; \quad \mathbf{R}^{\mu} = \mathbf{L}^{\mu} = \frac{\partial f}{\partial \boldsymbol{\mu}} = \mathbf{n}^{\mu} = \frac{b_1 \boldsymbol{\mu}}{[\tilde{J}_2]^{1/2}}$$

in which: $\mathbf{n}^{\sigma} = \dfrac{\tilde{\mathbf{s}}}{[\tilde{J}_2]^{1/2}}$

It is note that $\mathbf{n}^{\sigma}$ is the deviatoric part of the gradient of yield function with respect to Cauchy stress, i.e. $\mathbf{L}^{\sigma} = \dfrac{\partial f}{\partial \boldsymbol{\sigma}} = \mathbf{n}^{\sigma} - \dfrac{1}{3}N^{\sigma}\mathbf{I}$; $N^{\sigma} = \mathbf{n}^{\sigma}:\boldsymbol{\alpha} + \sqrt{\dfrac{2}{3}}\, m$. The dilatancy ratio, D, is related to plastic volumetric strain through the following equation

$$\dot{\varepsilon}_v^p = \langle L \rangle D \tag{16}$$

in which D is defined as

$$D = A_d(\boldsymbol{\alpha}_{\theta}^{d} - \boldsymbol{\alpha}):\mathbf{n}^{\sigma} \tag{17}$$

where $\boldsymbol{\alpha}_{\theta}^{d}$ is defined similar to the equations proposed by Manzari and Dafalias (1997) and Dafalias and Manzari (2004), i.e.

$$\boldsymbol{\alpha}_{\theta}^{d} = \sqrt{2/3}[g(\theta, c)M\exp(n^{d}\psi) - m]\mathbf{n}^{\sigma} \tag{18}$$

$$A_d = A_0(1 + \langle \mathbf{z}:\mathbf{n}^{\sigma} \rangle) \tag{19}$$

In Eq. (18), parameter M is the shear stress ratio at critical state, and n^d is a model constant. A key feature of Eq. (18) is the presence of state parameter, $\psi = e - e_c$, which makes dilatancy (D) a function of the distance between current void ratio (e) and the critical state void ratio (e_c) corresponding to the current mean effective stress (p). $\mathbf{z}$ is the fabric-dilatancy tensor which is the key element in capturing the response of sand in reverse loading (Dafalias and Manzari 2004). θ is a modified Lode angle defined as

$$\theta = \frac{1}{3}\sin^{-1}\left(\frac{-3\sqrt{3}}{2}\frac{J_{3s}}{J_{2s}^{3/2}}\right); \quad -\frac{\pi}{6} \le \theta \le \frac{\pi}{6} \tag{20}$$

where the terms J_{2s} and J_{3s} are the second and third invariant of the symmetric part of deviatoric (force-) stress tensor. The term $g(\theta, c)$ in Eq. (18) is a function used to represent the variation of soil dilatancy with the angle (θ). It is a function of $c = M_e / M_c$, the ratio between the slope of critical state line (in q-p' space) in triaxial compression and that in triaxial extension and θ

$$g(\theta, c) = \frac{2c}{(1+c) - (1-c)\cos 3\theta} \tag{21}$$

For $\theta = 0$ and $\pi/3$, the above equation yields $g = 1$ and $g = c$, respectively.

3.5 Hardening law

The evolution law for the back stress ratio tensor, α, is defined in the same way as proposed in Manzari and Dafalias (1997), i.e.

$$\dot{\alpha} = \langle L \rangle (2/3) h (\alpha_\theta^b - \alpha) \tag{22}$$

where
$$h = b_0 / (\alpha - \alpha_{in}) \mathbf{n}^\sigma \tag{23}$$

Alternatively, one may choose
$$h = \frac{b_0}{b_{ref} - \mathbf{b} : \mathbf{n}^\sigma} \tag{24}$$

in which: $\mathbf{b} = \alpha_\theta^b - \alpha$. The b_{ref} is either the "diameter" of the bounding surface along $\mathbf{n}^\sigma$, or $b_{ref} = \mathbf{b}_{\text{in}} : \mathbf{n}^\sigma$, where $\mathbf{b}_{\text{in}}$ is the initial value of $\mathbf{b}$ at the initiation of a loading process (they correspond to $b_{ref} = 2\text{M}^{\text{b}}$ or $b_{ref} = \text{b}_{\text{in}}$ of the triaxial formulation). The following relations are used for $\mathbf{b}_0$ and α_θ^b

$$b_0 = G_0 h_0 (1 - c_h e) (p / p_{at})^{-1/2} \tag{25}$$

$$\alpha_\theta^b = \sqrt{2/3} [g(\theta, c) M \exp(-n^b \psi) - m] \mathbf{n}^\sigma \tag{26}$$

h_0, G_0, c_h and n^b are model parameters.

Moreover, we use the relation proposed in Dafalias and Manzari (2004) to define the evolution of fabric-dilatancy tensor, $\mathbf{z}$

$$\dot{\mathbf{z}} = -c_z \langle -d\varepsilon_v^p \rangle (z_{\max} \mathbf{n}^\sigma + \mathbf{z}) \tag{27}$$

where c_z and $Z_{\max}$ are model parameters.

4. Finite element formulations

In a quasi-static regime, ignoring the body couples, the incremental form of the principles of virtual work is applied to the balance laws for soil skeleton (Eq. (4)) which yields

$$\int_\Omega \dot{\sigma}_{ij} \delta\dot{\varepsilon}_{ij} dV + \int_\Omega \dot{\mu}_{ij} \delta\dot{\kappa}_{ij} dV = \int_{\partial_1\Omega} \dot{t}_i \delta\dot{u}_i dA + \int_{\partial_2\Omega} \dot{m}_i \delta\dot{\phi}_i dA + \int_{\partial_2\Omega} \dot{b}_i \delta\dot{u}_i dV \tag{28}$$

where $\dot{t}_i$, $\dot{m}_i$ and $\dot{b}_i$ denote the components of traction, moment, and body force vectors respectively. δ denotes the virtual quantity. The right hand side terms in Eq. (28) represent the external virtual work components while the left hand side terms indicate the internal virtual work. Applying the effective stress concept, $\sigma_{ij} = \sigma'_{ij} + p\delta_{ij}$, the first term in Eq. (28) is split into two terms

$$\int_\Omega (\sigma'_{ij} + \dot{p}\delta_{ij}) \delta\dot{\varepsilon}_{ij} dV = \int_\Omega \sigma'_{ij} \delta\dot{\varepsilon}_{ij} dV + \int_\Omega \dot{p} \delta\dot{\varepsilon}_{ii} dV \tag{29}$$

Now Eq. (29) takes the form

$$\int_{\Omega} \dot{\sigma}_{ij}\delta\dot{\varepsilon}_{ij}dV + \int_{\Omega} \dot{p}\,\delta\dot{\varepsilon}_{ii}dV + \int_{\Omega} \dot{\mu}_{ij}\delta\dot{\kappa}_{ij}dV = \int_{\Gamma_\sigma} \dot{t}_i\delta\dot{u}_i dA + \int_{\Gamma_\mu} \dot{m}_i\delta\dot{\phi}_i dA + \int_{\Omega} \dot{b}_i\delta\dot{u}_i dV \tag{30}$$

Applying the virtual complementary work corresponding to the mass balance equations (Eq. (5)) we have for a time interval Δt

$$-\int_{\Omega} \delta\dot{p}(\dot{\varepsilon}_{ii}\Delta t)dV = \int_{\Omega} \delta\dot{p}\,\dot{\varepsilon}_{ii}dV - \int_{\Gamma_v} \delta\dot{p}(\dot{q}\Delta t)dA \tag{31}$$

The right side terms of Eq. (31) are the external virtual complementary work and the left side is the internal counterpart.

In the spatial discretization of the Eqs. (30) and (31) we define the distribution of displacements, rotations, and pore water pressure within the domain of the finite element as

$$\begin{aligned} u_i &= N^u_{iI}U_I; \quad \delta u_i = N^u_{iI}\delta U_I \qquad \text{where } i = 1,2,3; \quad I = 1,2,\ldots,3N^e_u \\ \phi_i &= N^\phi_{iI}\Phi_I; \quad \delta\phi_i = N^\phi_{iI}\delta\Phi_I \qquad \text{where } i = 1,2,3; \quad I = 1,2,\ldots,3N^e_\phi \\ p &= N^p_I P_I; \quad \delta p = N^p_I\delta P_I \qquad \text{where } I = 1,2,\ldots,N^e_p \end{aligned} \tag{32}$$

where N^u_{iI}, N^u_{iI}, and N^p_I are the interpolation functions corresponding to displacements u_i, rotation ϕ_i and pore water pressure p. The former two are vector functions of spatial coordinates while p is a scalar function of spatial coordinates. The total number of nodal points associated with u, ϕ, and p are given by N^e_u, N^e_ϕ and N^e_p respectively. U_I, Φ_I and P_I are the vectors of nodal values for displacements, rotations and pore water pressure associated with the element.

The rate forms of strain-displacement and curvature-rotation relationship are given by

$$\begin{aligned} \dot{\varepsilon}_{ij} &= \dot{u}_{j,i} - \Gamma_{ijk}\dot{\phi}_k; \qquad \delta\dot{\varepsilon}_{ij} = \delta\dot{u}_{j,i} - \Gamma_{ijk}\delta\dot{\phi}_k \\ \dot{\kappa}_{ij} &= \dot{\phi}_{j,i}; \qquad \delta\dot{\kappa}_{ij} = \delta\dot{\phi}_{j,i} \end{aligned} \tag{33}$$

Then using the relations in Eq. (32) we can write

$$\begin{aligned} \dot{\varepsilon}_{ij} &= B^u_{jiI}\dot{U}_I - \Gamma_{ijk}N^\phi_{kI}\dot{\Phi}_I; \qquad \delta\dot{\varepsilon}_{ij} = B^u_{jiI}\delta\dot{U}_I - \Gamma_{ijk}N^\phi_{kI}\delta\dot{\Phi}_I \\ \dot{\kappa}_{ij} &= B^\phi_{jiI}\dot{\Phi}_I; \qquad \delta\dot{\kappa}_{ij} = B^\phi_{jiI}\delta\dot{\Phi}_I \end{aligned} \tag{34}$$

where

$$B^u_{jiI} = N^u_{jL,i}; \qquad B^\phi_{jiL} = N^\phi_{jL,i}; \qquad B^p_{jL} = N^p_{L,j} \tag{35}$$

An implicit one-step scheme (θ-method) is used for temporal discretization of Eq. (5) which for time interval from t to $t+\Delta t$ is given by

$$\int_t^{t+\Delta t} f(\tau)d\tau = \theta\Delta t f(t+\Delta t) + (1-\theta)\Delta t f(t) \tag{36}$$

where the time dependent function $f(t)$ marches from t to $t+\Delta t$, and θ (assumed to be 1) is the time integration constant.

After spatial and time integrations of the governing equations its final form is obtained as

$$\begin{bmatrix} K_{LI}^{uu} & K_{LJ}^{u\phi} & K_{LK}^{up} \\ K_{MI}^{\phi u} & K_{MJ}^{\phi\phi} & 0 \\ K_{NI}^{pu} & 0 & 0 \end{bmatrix} \begin{bmatrix} \Delta U_I \\ \Delta \Phi_j \\ \Delta P_K \end{bmatrix} + \begin{bmatrix} 0 & 0 & 0 \\ 0 & 0 & 0 \\ 0 & 0 & \Delta t K_{NK}^{pp} \end{bmatrix} \begin{bmatrix} U_I \\ \Phi_j \\ P_K \end{bmatrix} = \begin{bmatrix} \Delta F_L^u \\ \Delta F_M^\phi \\ \Delta t F_N^p \end{bmatrix} \tag{37}$$

where the respective stiffness matrices are given as

$$\begin{aligned} K_{LI}^{uu} &= \int_\Omega B_{jiL}^u \mathcal{D}_{ijkl}^{ep} B_{lkI}^u dV \\ K_{LJ}^{u\phi} &= \int_\Omega B_{jiL}^u \mathcal{L}_{ijkl}^{ep} B_{lkJ}^\phi dV - \int_\Omega B_{jiL}^u \mathcal{D}_{ijkl}^{ep} \Gamma_{kls} N_{sJ}^\phi dV \\ K_{MI}^{\phi u} &= \int_\Omega B_{jiM}^\phi \mathcal{E}_{ijkl}^{ep} B_{lkI}^u dV - \int_\Omega \Gamma_{ijs} N_{sM}^\phi \mathcal{D}_{ijkl}^{ep} B_{lkI}^u dV \\ K_{MJ}^{\phi\phi} &= \int_\Omega \Gamma_{ijs} N_{sM}^\phi \mathcal{D}_{ijkl}^{ep} \Gamma_{klr} N_{rJ}^\phi dV - \int_\Omega B_{jiM}^\phi \mathcal{E}_{ijkl}^{ep} \Gamma_{kls} N_{sJ}^\phi dV \\ &\quad + \int_\Omega B_{jiM}^\phi \mathcal{M}_{ijkl}^{ep} B_{lkJ}^\phi dV - \int_\Omega \Gamma_{ijs} N_{sM}^\phi \mathcal{L}_{ijkl}^{ep} B_{lkJ}^\phi dV \\ K_{LK}^{up} &= \int_\Omega B_{jiL}^u m_{ij} N_k^p dV; \quad K_{LK}^{pu} = (K_{LK}^{pu})^T \\ K_{NK}^{pp} &= -\frac{1}{\gamma_w} \int_\Omega B_{jN}^p k_{ij} B_{iK}^p dV \end{aligned} \tag{38}$$

where m_{ij} is an identity tensor due to the volumetric strain. The respective external force vectors on the right hand side of Eq. (37) are given by

$$\begin{aligned} \Delta F_K^u &= \int_{\Gamma_\sigma} \Delta t_i N_{iK}^u dA + \int_\Omega \Delta b_i N_{iK}^u dV \\ \Delta F_L^\phi &= \int_{\Gamma_\mu} \Delta m_i N_{iL}^\phi dA \\ F_N^p &= \int_{\Gamma_p} q N_L^p dA + \frac{1}{\gamma_w} \int_\Omega B_{jN}^p k_{ij} b_i^w dV \end{aligned} \tag{39}$$

There is coupling between displacement and rotation, and displacement and pore water pressure, but no coupling exists between rotation and pore water pressure.

Eq. (37) is the governing equations at the element level. At the structural level the global stiffness matrix, force vector, and the vector of unknowns are assembled and the global system of equations are solved employing a commonly used Newton-Raphson technique. For dry soils, Eq. (37) can be reduced to u-ϕ case by omitting the terms corresponding to pore water pressure.

The critical state micropolar plasticity model and the two finite element formulations (u-ϕ and u-ϕ-p) are implemented in the commercial finite element code, ABAQUS, via a user-defined subroutine, UEL (HKS 2010). For the plane strain simulations reported in this paper, u_8-ϕ_4 and u_8-

ϕ_4-p_4 have been used. Triangular finite elements including u_6-ϕ_3 and u_6-ϕ_3-p_3 have also been implemented and successfully tested (Yonten and Manzari 2010). The u_8-ϕ_4 element uses bi-quadratic shape functions for displacements and bilinear shape functions for micro-rotation. The u_8-ϕ_4-p_4 uses bilinear shape functions for both the micro-rotation and pore water pressure.

5. Numerical simulations

5.1 Mesh objectivity

Before conducting the simulations for Toyoura sand, a simplified version of the micropolar model was tested for mesh objectivity at the post-failure regime. This was done by using three different meshes of a $4^{cm} \times 14^{cm}$ biaxial specimen of soil with a peak friction angle of 40 degrees and a critical state friction angle of 30 degrees. Soil dilation angle was assumed to vary from 25 degrees at the peak to zero at critical state. The elastic modulus and Poisson's ratio were set to be 11920 kN/m^2 and 0.25, respectively. A length scale of $l_1 = l_2 = 1$ mm was used in the simulations.

Fig. 1 shows the finite element meshes used along with the imperfection introduced to trigger shear localization. The imperfection is introduced through a reduced value of soil cohesion in the elements displayed by black color in the Figure. The force displacement curves for the three meshes are presented in Fig. 2. As it can be seen the force displacement curves are nearly identical, suggesting the objectivity of the micropolar regularization in the post-failure regime.

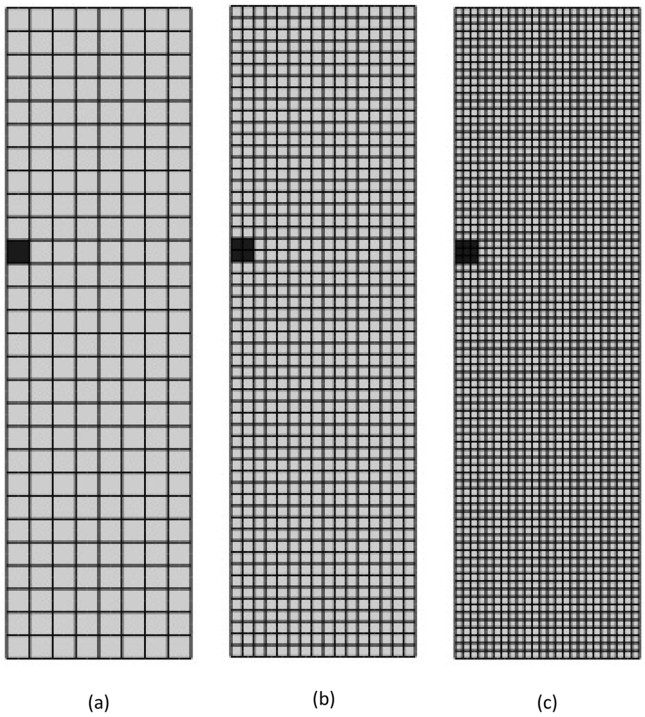

Fig. 1 Finite element meshes (u_8-ϕ_4): (a) 8x28, (b) 16x56, and (c) 24x84

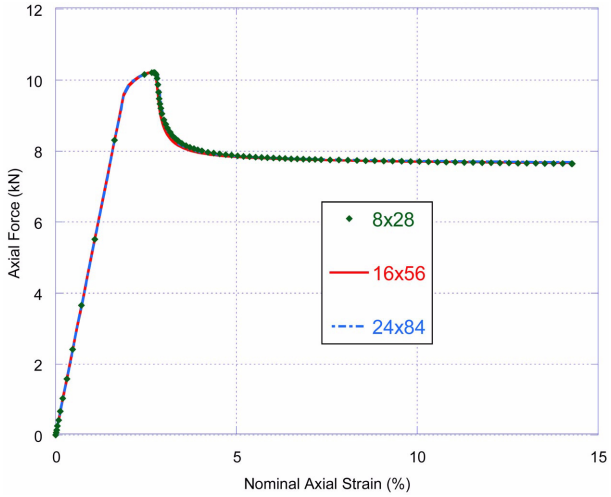

Fig. 2 Force displacement curves obtained by using the three different meshes shown in Fig. 1

Table 1 Model parameters

Elastic	G_o	125 kPa
	ν	0.05
Critical state	M	1.25
	λ_c	0.019
	e_o	0.934
	ξ	0.7
Yield surface	m	0.01
State parameters	n^b	1.1
	n^d	3.5
Hardening	h_o	7.05
	c_h	0.968
Dilatancy	A_o	0.704
Fabric-dilatancy	z_{max}	4
	c_z	600

5.2 Simulation of toyora sand in biaxial compression

Next, a $4^{cm} \times 14^{cm}$ biaxial specimen of Toyoura sand is considered. Given the results of the simulations shown in Fig. 2, the finite element meshes used in these simulations consisted of 228 u_8-ϕ_4 elements for drained compression test and 228 u_8-ϕ_4-p_4 elements for undrained compression.

These simulations were conducted for a relatively dense specimen of Toyoura sand that is slightly heterogeneous with an average initial void ratio of 0.735 (Dr = 63%). Initial void ratios of the specimen at different integration points within the elements were randomly assigned using a random number generator. The average void ratio is 0.735 with a variance of 0.01. The random distribution of initial void ratios within the specimen is shown in Fig. 3. The values of initial void ratios vary from 0.725 to 0.745. All non-polar model parameters are the same as those proposed in Dafalias and Manzari (2004) for Toyoura sand and are given in Table 1.

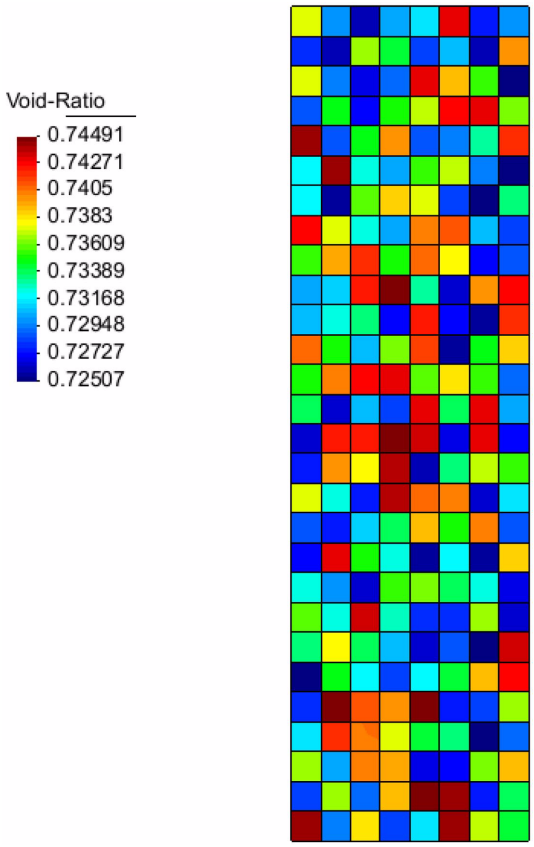

Fig. 3 Random distribution of initial void ratios within the soil specimen

The micro-rotations (ϕ_z) at the top and bottom edges of the specimen are fixed. The specimen is isotropically consolidated first by applying a confining pressure of 100 kPa. Then the soil specimen is sheared by applying a vertical displacement of 3 cm on the top edge. It is important to note that the numerical simulations presented in the following sections are strictly valid for small strain/small displacement regime. In most cases, however, as shear strains become localized, large strains may eventually develop in the localized zone. Hence, the distributions of strains and curvatures within the soil specimen and evolution of theses quantities throughout the test, not the exact magnitudes of these strains and curvatures, will be of main concern in the following sections.

5.2.1 Drained compression results

Two drained biaxial simulations were conducted, one using a classical Cauchy continuum, and another using a micropolar continuum with a length scale of $l_1 = l_2 = 4$ mm.

Fig. 4 shows the force-displacement curves obtained for the two simulations. It is observed that with the classical Cauchy continuum the finite element simulation stops prematurely due to numerical divergence. This is a typical behavior, often observed in the standard finite element simulation of boundary value problems involving shear localization. The initial boundary value problem based on the classical Cauchy continuum becomes ill-posed as localized shear zones start

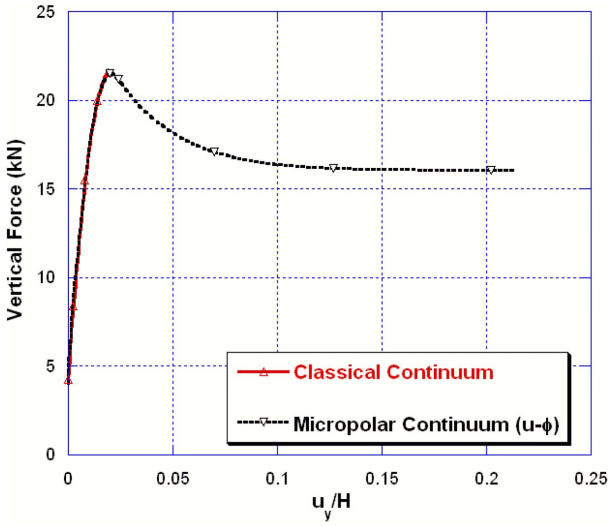

Fig. 4 Comparison of simulation of a drained biaxial specimen of Toyoura sand (initial confining pressure = 100 kPa, initial average void ratio = 0.735) using classical continuum and the two-scale micropolar elastoplastic model

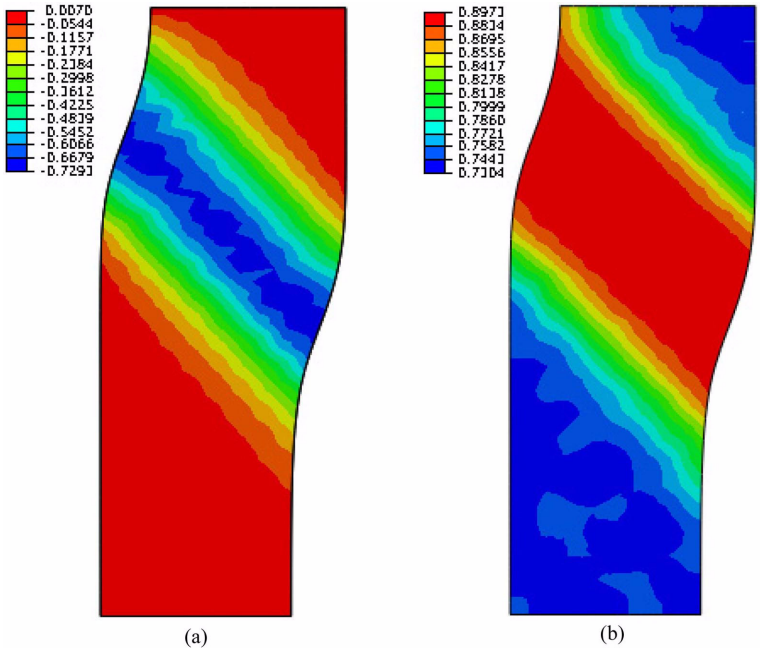

Fig. 5 (a) The micro-rotation and (b) void ratio distributions within the soil specimen at the end of drained micropolar simulation with a length scale of 4 mm

to emerge. On the other hand, the micropolar simulation with the length scale of 4 mm was able to fully regularize the boundary value problem and allowed for a complete solution in the post peak regime.

Fig. 5 shows the contour plots of micro-rotations (a) and void ratios (b) within the soil specimen

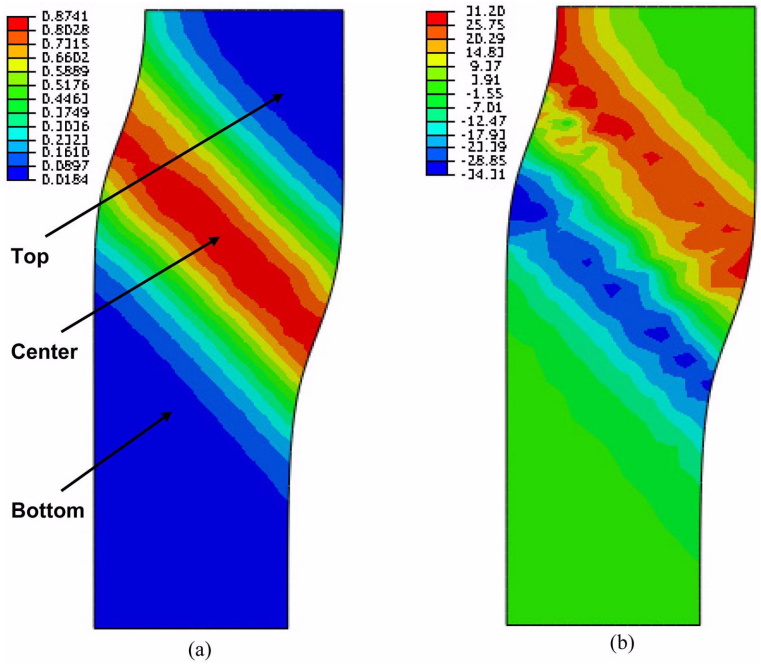

Fig. 6 (a) The equivalent plastic strain and (b) curvature, κ_{yz} distributions within the soil specimen at the end of drained micropolar simulation with a length scale of 4 mm

at the end of micropolar simulation. The micro-rotations are significantly larger at the center of the localized zone and negligible outside the zone. This indicates that micro-rotations are active only in the shear band where grain rotation is significant. The void ratio of the soil at the localized zone has increased significantly as the soil in that region dilated toward a critical state condition. The void ratio outside the localized zone remained almost the same as its initial values (Fig. 5(b)).

Fig. 6 shows the contour plots of equivalent plastic strains (a) and curvature, κ_{yz} (b) at the end of the simulation. The equivalent plastic strains are significantly larger at the center of the localized zone compared to the regions outside the zone. Similarly, the curvature is also larger at the localized zone than outside of it. The curvatures above the center of the localized zone are positive while those below the center have negative signs. This shows that inside the localized zone the grains rotate in opposite directions.

To observe the soil response during strain localization evolution of some important physical quantities is investigated at three points in the specimen as shown in Fig. 6(a). The first point is below the localized zone, a second one is at the center of the zone and the third is above the zone. The evolutions of micro-rotations and void ratios are shown in Figs. 7 and 8. The micro-rotations below and above the localized zone are insignificant while at the center of the zone reaches about 41 degrees at the end of the simulation. Similarly, the changes in the void ratios outside the localized zone are negligible while at the center the void ratio increases to 0.895 at the end of the simulation. The soil at the three regions initially contracts before dilating. The curvatures outside the localized zone have opposite signs and reach the same magnitude towards the end of the simulation. The curvatures at the center of the zone steadily increased in the positive direction.

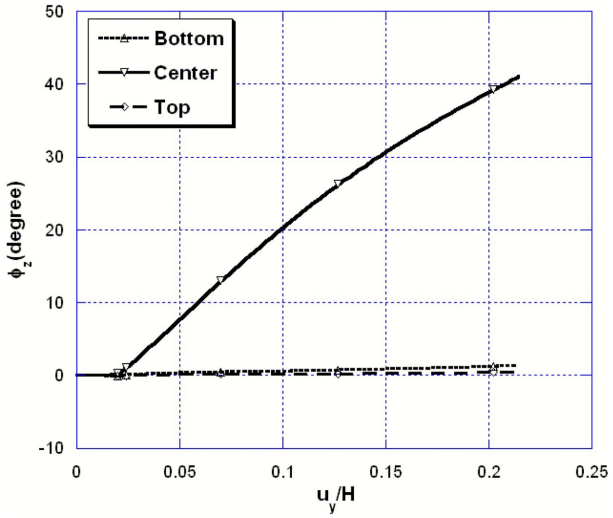

Fig. 7 Evolution of micro-rotation at the bottom, center and top (as shown in Fig. 6(a)) of the localized zone in a drained biaxial simulation

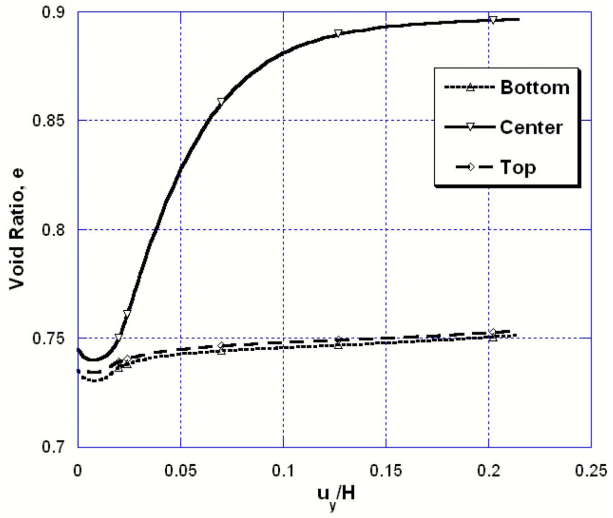

Fig. 8 Evolution of void ratio at the bottom, center and top (as shown in Fig. 6(a)) of the localized zone in a drained biaxial simulation

5.2.2 Undrained compression results

In an undrained biaxial compression simulation the pore water is prevented from seeping out at the boundaries of the soil specimen, but it is allowed to flow within the specimen. Therefore, it is undrained in a global sense. Two simulations are conducted, one using the fully-coupled classical continuum (u-p) and the other using fully-coupled micropolar continuum (u-ϕ-p) with a length scale of $l_1 = l_2 = 1$ mm.

Fig. 9 shows the force-displacement curves for the two simulations. Unlike in the drained case the fully-coupled Cauchy continuum allows the finite element simulation to continue beyond the onset

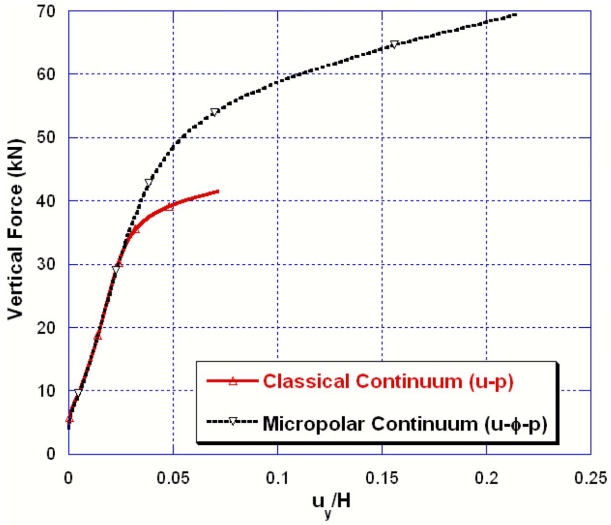

Fig. 9 Comparison of simulation of an undrained biaxial specimen of Toyoura sand (initial confining pressure = 100 kPa, initial average void ratio = 0.735) using classical continuum and the two-scale micropolar elastoplastic model

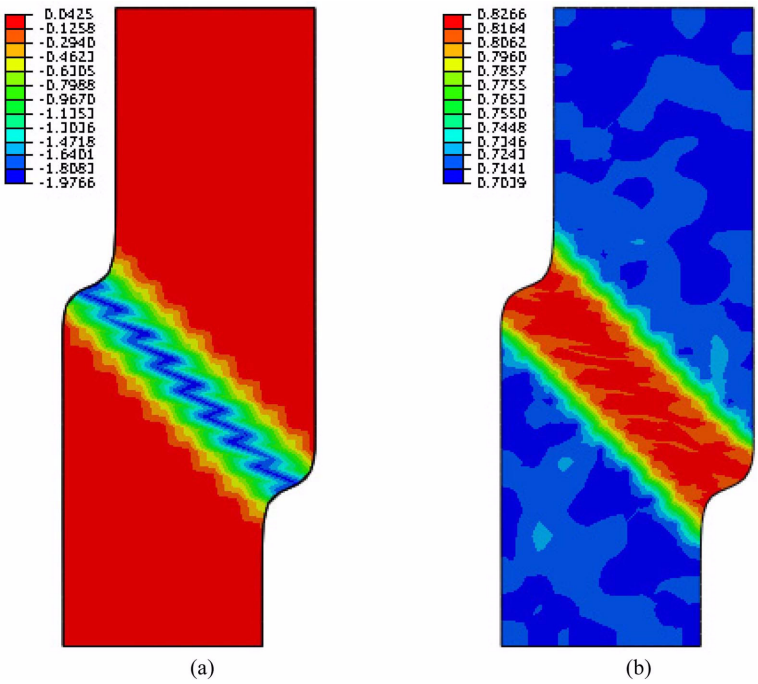

Fig. 10 (a) The micro-rotation and (b) void ratio distributions within the soil specimen at the end of undrained micropolar simulation with a length scale of 1 mm

of localization and reach up to 7% nominal strain. This is because in a saturated soil the fluid viscosity has some regularizing effect. However, after the onset of localization the curve deviates

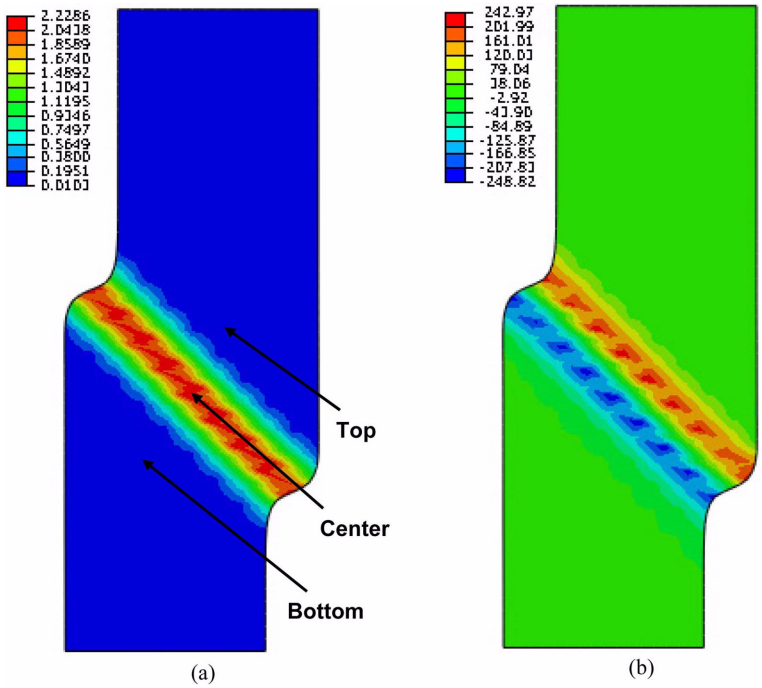

Fig. 11 (a) The equivalent plastic strain and (b) curvature, κ_{yz} distributions within the soil specimen at the end of undrained micropolar simulation with a length scale of 1 mm

from that of the micropolar continuum. This is expected because the classical continuum solution is mesh-dependent due to the lack of an internal length scale. For the micropolar continuum regularization takes place at two levels, one due to fluid viscosity and the other due to the micropolar features.

Fig. 10 shows the contour plots of micro-rotations (a) and void ratios (b) within the soil specimen at the end of micropolar simulation. At the center of the localized zone the micro-rotations are significantly larger than outside the zone. Similarly, the void ratio of the soil at the localized zone increases causing significant dilation in that region. However, the void ratio outside the localized zone slightly decreases showing contractive behavior (Fig. 10(b)).

Fig. 11 shows the contour plots of equivalent plastic strains (a) and curvature, κ_{yz} (b) at the end of the simulation. As expected the localized zone undergoes large plastic straining as shown by significantly large values of the equivalent plastic strains. Similarly, the curvature is also larger at the localized zone than outside it. The rotation of the grains in the opposite directions at the localized zone is indicated by the splitting of the curvatures at the center into opposite signs.

Three points in the specimen, one below, a second at the center and the third above the localized zone are selected to gain further insights into soil response during localization. The locations of these points are shown in Fig. 11(a). The evolutions of micro-rotations, void ratios are shown in Figs. 12-13. The micro-rotations, void ratios, and curvatures below and above the localized zone do not evolve insignificantly. However, at the center of the zone the values of micro-rotations, void ratios and curvatures become significantly larger. Fig. 14 shows the stress paths at the bottom, center and top of the localized zone in the undrained biaxial simulations reported in Fig. 10. It is

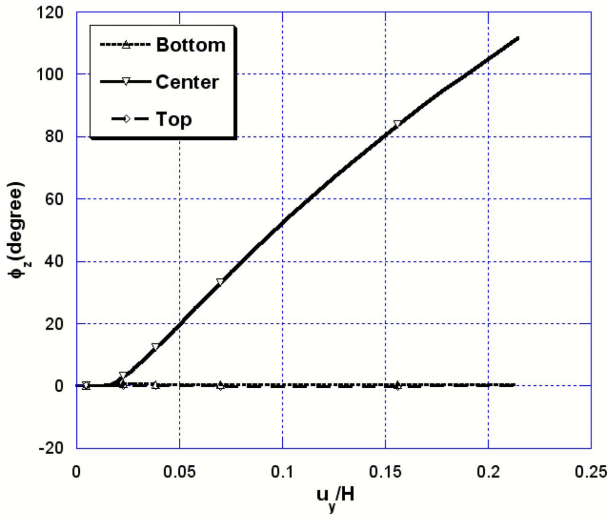

Fig. 12 Evolution of micro-rotation at the bottom, center and top (as shown in Fig. 11(a)) of the localized zone in an undrained biaxial simulation

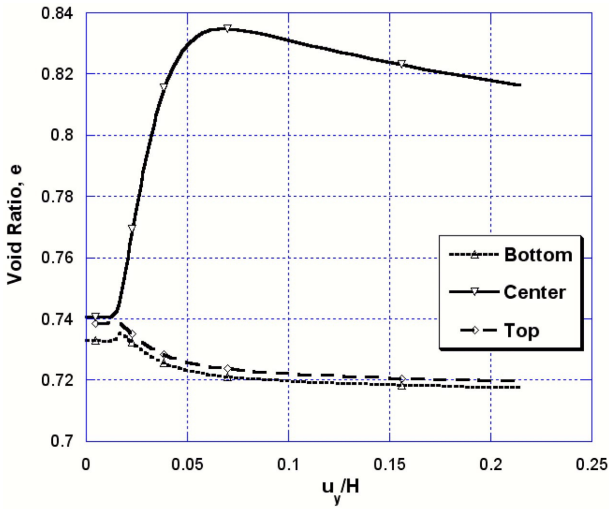

Fig. 13 Evolution of void ratio at the bottom, center and top (as shown in Fig. 11(a)) of the localized zone in an undrained biaxial simulation

clear that the stress path in the center element is clearly deviated due to enhanced softening in the localized zone.

A comparison of the undrained simulations presented in this section with the drained simulation results presented in section 5.2.1 shows that in both cases the slightly heterogeneous soil specimen develop a localized shear band at which void ratio is significantly increased due to the large shear-induced volume change in the material. In the drained condition, this dilation leads to strain softening manifested in the decreasing strength of the soil (Fig. 4) while in undrained condition it causes significant negative pore pressure leading to an increase in the soil strength. Comparing Figs.

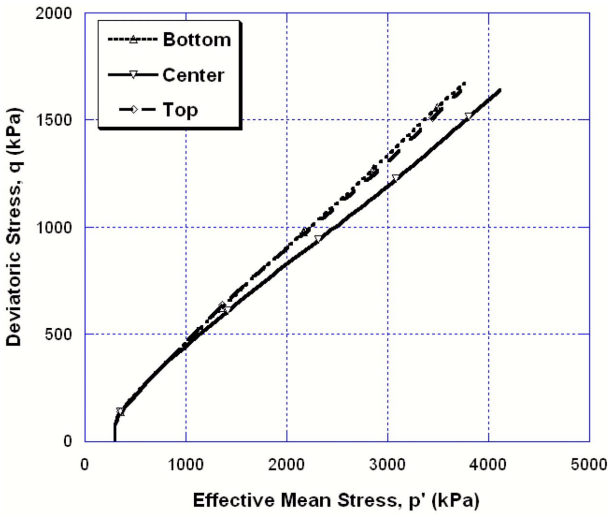

Fig. 14 Effective stress paths computed at the bottom, center, and top (as shown in Fig. 11(a)) of the localized zone in an undrained biaxial simulation

6(a) and 11(a) also confirms that selection of a larger length scale (4^{mm} versus 1^{mm}) leads to thicker shear band in the soil specimen.

6. Conclusions

The two-scale micropolar elastoplastic constitutive model used in this work is able to simulate the response of slightly heterogeneous specimens of granular soils in both pre- and post peak regimes in drained and undrained conditions. In a drained simulation the classical continuum counter-part of the model provides an almost identical response in the pre-peak part of the force-displacement response, but fails to provide convergent solution beyond the maximum force taken by the specimen. In an undrained simulation due to regularizing effect of fluid viscosity the classical continuum is able to continue after the onset of localization, however, it is well-known that it produces mesh-dependent solution. The micropolar model is able to capture the response of the soil at the localized zone where grain rotations and dilation are significant.

Acknowledgements

This work is supported by the National Science Foundation Geomechanics and Geohazard programs directed by Dr. Richard Fragaszy. This support is gratefully acknowledged.

References

Alsaleh, M., Voyiadjis, G.Z. and Alshibli, K.A. (2006), "Modelling strain localization in granular materials using micropolar theory: mathematical formulations", *Int. J. Numer. Anal. Meth. Geomech.*, **30**(15), 1501-1524.
Alsaleh, M., Kitsabunnarat, A. and Helwany, S. (2009), "Strain localization and failure load predictions of

geosynthetic reinforced soil structures", *Interact. Multiscale Mech.*, **2**(3), 235-261.
Alshibli, K.A., Alsaleh, M. and Voyiadjis, G.Z. (2006), "Modelling strain localization in granular materials using micropolar theory: numerical implementation and verification", *Int. J. Numer. Anal. Meth. Geomech.*, **30**(15), 1525-1544.
Alshibli, K.A. and Sture, S. (2000), "Shear band formation in plane strain experiments of sand", *J. Geotech. Geoenv. Eng.*, **126**(6), 495-503.
Dafalias, Y.F. and Manzari, M.T. (2004), "A simple plasticity sand model accounting for fabric change effects", *J. Eng. Mech. - ASCE*, **130**(6), 622-634.
Forest, S. (2001), *Cosserat media, in encyclopedia of materials: science and technology*, Elsevier Sciences Ltd., 1715-1718.
Hibbitt, Karlsson & Sorensen Inc (HKS) (2010), *ABAQUS/Standard user subroutine reference manual, version 6.10*, HKS, Providence, R.I. 2010.
Huang, W. and Bauer, E. (2003), "Numerical investigations of shear localization in a micro-polar hypoplastic material", *Int. J. Numer. Anal. Meth. Geomech.*, **27**, 325-352
Lade, P.V. and Kim, M.K. (1998). "Single hardening plasticity model for frictional materials", *Comput. Geotech.*, **6**, 13-29.
Manzari, M.T. and Dafalias, Y.F. (1997), "A critical state two-surface plasticity model for sands", *Geotechnique*, **47**(2), 255-272.
Manzari, M.T. (2004), "Application of micropolar plasticity to post failure analysis in Geomechanics," *Int. J. Numer. Anal. Meth. Geomech.*, **28**(10), 1011-1032.
Manzari, M.T. and Dafalias, Y.F. (2005), "A critical state two-surface micropolar plasticity model for sands", *Proceedings of 11th International Conference on Fracture*, Turin, Italy, March, 2005.
Nowacki, W. (1986), *Theory of asymmetric elasticity*, Pergamon Press, New York.
Vardoulakis, I. and Sulem, J. (1995), *Bifurcation analysis in geomechanics*, Blackie Academic and Professional, Chapman and Hall, Glasgow.
Viggiani, G., Besuelle, P., Hall, S. and Desrues, J. (2010), "Sand deformation at the grain scale quantified through x-ray imaging", *Proceedings of 3rd International Workshop on X-Ray CT for Geomaterials*, GeoX 2010, ISTE Pub., New-Orleans, USA, March 1-3, 2010.
Yonten, K. and Manzari, M.T. (2010), "On micropolar finite element analysis using a two-scale constitutive model", *Proceedings of 16th US National Congress of Theoretical and Applied Mechanics*, Pennsylvania, USA, June 27-July 2, 2010.